

## Research Paper

# 3D printed three-dimensional metallic microlattices with controlled and tunable mechanical properties

Mohammad Sadeq Saleh<sup>a,1</sup>, Chunshan Hu<sup>a,1</sup>, Jacob Brenneman<sup>a</sup>, Al Muntasar Al Mutairi<sup>b</sup>, Rahul Panat<sup>a,\*</sup>

<sup>a</sup> Department of Mechanical Engineering, Carnegie Mellon University, Pittsburgh, PA 15213, USA

<sup>b</sup> School of Mechanical and Materials Engineering, Washington State University, Pullman, WA 99164, USA

## ARTICLE INFO

## Keywords:

Additive manufacturing  
Aerosol jet printing  
3D metallic microlattices  
Controlled and tunable mechanical responses  
Finite element analysis  
Semi-empirical model

## ABSTRACT

Three-dimensional metallic microlattice structures are critical for advancements in areas such as energy storage and conversion, high-sensitivity sensors, light-weight structures, bone implants, and high-efficiency catalysts. In this paper, Aerosol Jet 3D nanoparticle printing (Saleh et al., 2017) [23] is utilized to fabricate novel highly complex three dimensional (3D) metallic microlattice materials having near-solid truss members with diameters of 30–60  $\mu\text{m}$  and unit sizes of 100–400  $\mu\text{m}$ . Three types of lattice structures having densities from 5% to 26% of the bulk metal are designed to deform via bending-dominated and buckling-dominated mechanisms under compressive loads. The mechanical response of these microlattices could be tuned by changing the structure density as well as making simple changes to the cell architecture. It is shown that AM related local defects in the 3D structures did not significantly influence their global stress-strain response. A modified semi-empirical foam deformation model is proposed to capture the oscillating hardening and softening mechanical behavior of ordered structures in the plateau stress region and is fit to all three lattice structures printed in this study. Finite Element Analysis (FEA) of the deformation using 3D beam elements was also performed, which showed an agreement with the experimental observations for both the global stress-strain response and the local deformation for structures that deform by bending. A theoretical model of general applicability is also proposed that captures the periodic hardening and softening behavior of the microlattice structures in the plateau region of their stress-strain plots. The research results establish that AJ printing can be used to fabricate a novel class of microlattice structures with tunable and controlled mechanical response.

## 1. Introduction

Several microlattice architectures with solid truss members form the basis of natural structures that have their properties optimized over millions of years via evolutionary changes. Materials such as trabecular bones, wood, and plant stems have microstructures that show a high degree of mechanical efficiency and energy absorption. Such structures are also believed to be key in developing engineering systems such as lightweight high-strength materials [1,2], materials with controlled deformation [3], fast-charging high-capacity Li-ion batteries [4], biomedical implants [5], catalysts [6], and microfilters. The manufacture of structures with precise microlattice architectures, however, is not straightforward and considerable efforts are spent by researchers to achieve the same. Although cellular structures can be fabricated using

conventional processes such as foaming [7], welding [8], sheet metal folding [9], and extrusion, they are limited in their ability to create controlled microscale features. Recent advances in additive manufacturing (AM), i.e., 3D printing, has led to several possibilities of fabricating 3D interconnects and lattice structures with a high precision. These processes include selective freeform printing [10–12], inkjet Printing (IJP) [13–15], laser sintering (SLS) [16], electron beam melting (EBM) [17], direct laser writing (DLW) [2], fused deposition modeling (FDM) [18], 2-photon lithography [19] and other templating methods [10,20]. The ability to fabricate microlattice structures with solid truss members using these methods, however, has been challenging. For example, 2-photon lithography [19] can create polymer 3D nano and microlattice structures that are coated with metals (or ceramics) using atomic layer deposition, before burnout of the polymer. This process

\* Corresponding author.

E-mail address: [rpanat@andrew.cmu.edu](mailto:rpanat@andrew.cmu.edu) (R. Panat).

<sup>1</sup> Equal contribution.

[19] creates precisely structured microlattices with hollow truss members. Note that solid truss members are needed in a class of applications, such as Li-ion batteries [4], where adequate mass loading of the members/lattice is necessary to have a practical range of the total energy storage capacity. Other examples where solid truss members are needed include lightweight structural materials that can absorb shocks and vibrations in aerospace applications [21] and hierarchical scaffold structures used as biomedical implants [22].

A gap thus exists in the fabrication of controlled metallic microlattice materials and structures with solid or near-solid truss members. Free-form fabrication of microlattices via a deposition of nanoparticle solutions and inks in 3D space without any support materials was enabled by our earlier work using Aerosol Jet-based additive manufacturing [23]. The printing process was followed by heating, which removed the binders in the lattice and caused the sintering of the nanoparticles. Although this work involved fabrication of such structures, the focus of our earlier work [23] was only on manufacturing process development and demonstrating a few representative structures. Note that Aerosol Jet (AJ) printing is a microscale 3D printing method that has been successfully used for the fabrication of a diverse set of 2D electronic devices and materials [4,23–26].

Designing the mechanical response of microlattice structures is important for the end applications and depends on various factors such as the size and shape of the unit cells, closed-cell vs open-cell structures, types of truss members (i.e. hollow, solid, or porous), and relative density of the lattice structure [27]. In addition, the properties are also expected to depend upon the types of defects within the microlattice structures. It is thus important for the fabrication processes to create various unit cell architectures that can tune the mechanical response with desired characteristics. Classification of lattices into bending or stretching-dominated structures have been proposed and extensively used to predict the mechanical strength and modulus of these structures given the relative density of the lattice [27,28]. Note that the upper bound of the mechanical strength and moduli of the lattice structures was described by Hashin et al. [29].

The bending-dominated cellular structures discussed in this work have excellent energy absorption characteristics and consequently several phenomenological models have been proposed to help predict their stress-strain behavior under uniaxial compression and have been validated by either experiments or numerical calculations [27,30–34]. Experiments show that under compression, stress-strain response of the cellular materials can be divided into three separate regions, namely, elastic region, a stress plateau region showing instabilities, and a densification region [27,30–34]. The first model that predicted the stress-strain relationship for cellular foams was proposed by Rusch et al. [35]. The Rusch model was later refined to enable a better fit of the predictions with the experimental data, especially in the elastic and stress plateau regions [36–40]. These models are developed for random foams and therefore do not predict the periodic softening and hardening behavior observed in the plateau region of the stress-strain curve of ordered cellular materials. In this work, an additional term is proposed to capture this periodic softening and hardening of ordered cellular materials.

The impetus for the current work is thus twofold. First, we wanted to demonstrate 3D metallic microlattice structures with near-solid truss members having controlled mechanical properties, thereby realizing novel structural materials. The focus was on demonstrating three types of silver microlattice structures that deform by bending-dominated mechanism with densities ranging between 5% and 26% of the bulk, where the structure controls their mechanical properties. In addition, we wanted to see if 3D printing offers the ability for a simple change to printing program to tune/change the mode of deformation for the microlattices. We aimed to make 3D microlattice structures with overall dimensions of a few millimeters with truss diameters in the range of 30–60  $\mu\text{m}$  and unit lattices in the range of 100–400  $\mu\text{m}$ ; a structural length scale important for multiple practical applications. The second

aim of the work was to measure the mechanical response of these structures and develop numerical and semi-empirical theoretical models that would capture/predict this behavior. This part of the work focused on correlating the mechanical response to specific microlattice structures and gaining an ability to predict the same via numerical and semi-empirical models.

## 2. Materials and methods

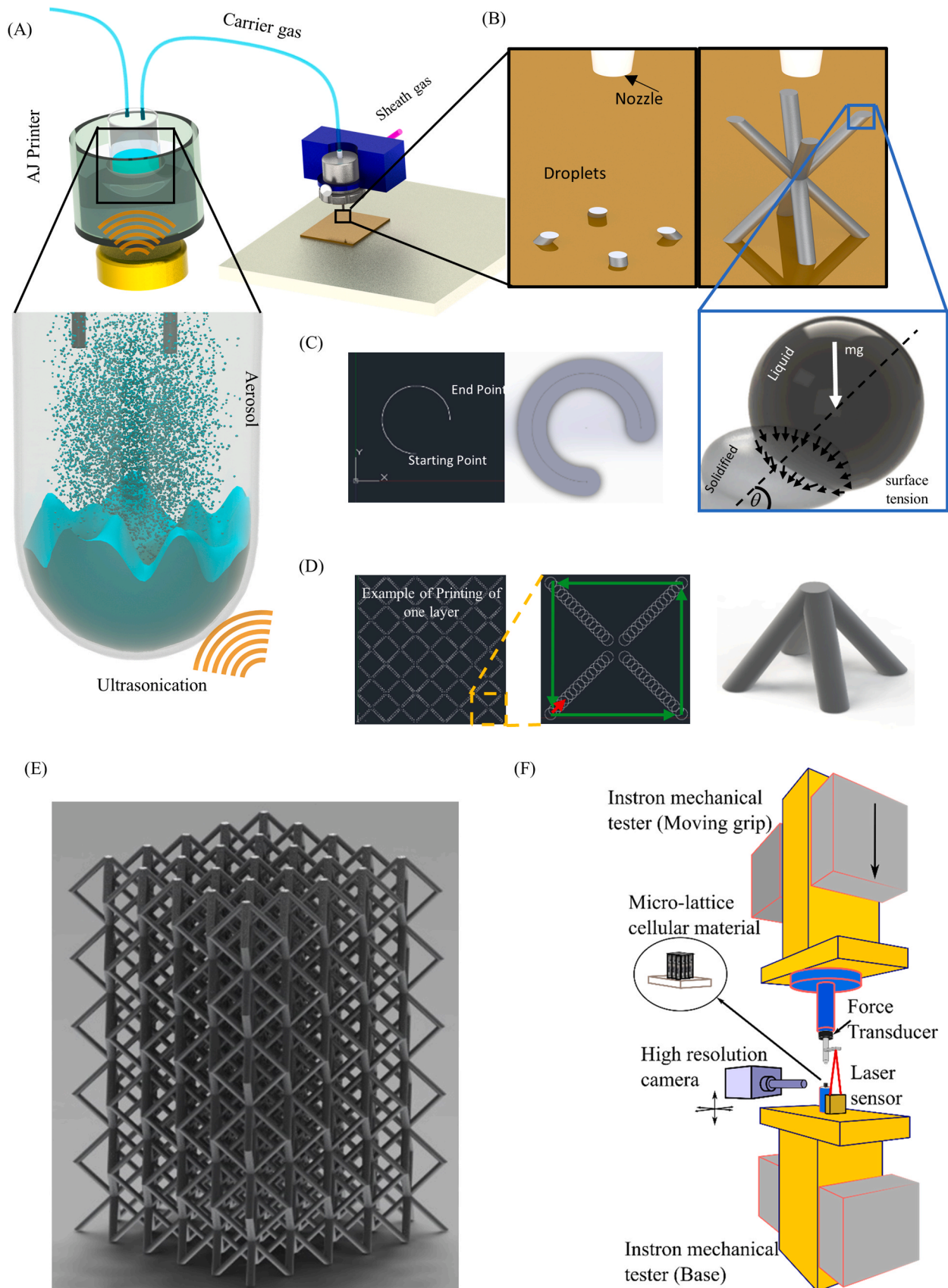
### 2.1. Materials

A commercial silver nanoparticle ink (Prelect TPS50, Clariant, Frankfurt, Germany) with density of 1.75 g/cm<sup>3</sup>, a particle size of 30–50 nm, and a particle loading of 40  $\pm$  2 wt% was utilized to form the 3-D microarchitectures. The ink was mixed with DI water at a ratio of 3:1 for printing.

### 2.2. Aerosol Jet printing

The 3D microlattice cellular structures were fabricated using AJ 3D printer (AJ300, Optomec Inc, Albuquerque, NM), which is a microscale additive manufacturing (AM) method. AJ printing is a continuous material jetting process that utilizes transformation of the inks into a mist of aerosol droplets (each droplet containing nanoparticles of the material in the ink - e.g., silver in our case) to be deposited at a desired location. The AJ machine used in this work had two types of atomizers, namely, ultrasonic and pneumatic, of which the ultrasonic atomizer was used due to its compatibility with the nanoparticle ink. The AJ printer also has a precisely controlled programmable XY stage, a deposition head, camera systems, and a heating element to control the temperature of the moving stage. In the printing process, Ag nanoparticle ink was atomized by ultrasonic energy and carried by N<sub>2</sub> gas to the deposition head in the form of an aerosol mist (Fig. 1A). The aerosol droplets were then focused by a sheath gas (also N<sub>2</sub>) through a ceramic nozzle onto a substrate. The standoff distance between nozzle tip and substrate was initially kept at about 3 mm. After every 500  $\mu\text{m}$  build-up of the structure, however, the deposition head was elevated by the same amount to maintain the working distance. Printing process was monitored through an optical camera (FL3-GE-13S2C, Point Grey, OR) attached to a beam which holds the deposition head. The droplet diameter after precipitation was measured using another optical camera (ANJU6186, Panasonic, Kadoma, Osaka Prefecture, Japan) on the AJ printer. The ceramic nozzles used in this study had a diameter of 150  $\mu\text{m}$ , which are known to generate an aerosol stream of about 15  $\mu\text{m}$  in diameter [41]. In order to achieve different global densities of the printed lattice, the printing design/path, and the carrier gas (22–28 sccm) and sheath gas pressures (45–55 sccm) were varied. Under the same printing speed and printing path, the higher sheath gas pressure resulted in lower diameters of the truss members, while the lower sheath gas pressure resulted in higher diameters of the truss members. Using this methodology, the diameters of the truss members of the scaffolds were varied between 30  $\mu\text{m}$  and 60  $\mu\text{m}$ . The printing parameters, however, needed to be optimized for silver nanoparticle ink manufacturer and batches within the ranges mentioned above to get the desired diameters of the truss members of the 3D structures shown in Fig. 1B. Another method to change the truss diameters was to change the radius of the semi-circular printing path shown in Fig. 1C. During the build-up of the structure, no support material was used as the surface forces shown in the inset of Fig. 1B were sufficient to hold the droplet in place before it dried-up due to the heat of the platen. As shown in our earlier work [23], the primary limitation of this method is that the three-dimensional truss members fabricated by this technique can have an angle between 37° and 90° to the horizontal.

Commercial software AutoCAD (Autodesk, San Rafael, CA) was used to generate the drawings for geometries of the 3D architectures. The drawings were transferred to a 'prg' format using VMTTools, which is an AutoCAD add-on from Optomec Inc that is compatible with the AJ



(caption on next page)

**Fig. 1. AJ printing of 3-D microlattices without support structures.** (A) Schematic of the operation of AJ 3D printer. Ultrasonic action creates microdroplets containing metal nanoparticles that are driven to a nozzle by carrier gas and focused on the substrate by sheath gas. (B) Schematic of droplet-by-droplet and layer-by-layer printing sequence (left) and the force balance mechanism between the solidified droplets and just-deposited liquid droplets. (C) Representative printing path drawn in AutoCAD (left) and a schematic of the printed structures based on the same (right). (D) An original 2-D AutoCAD design (left) and a zoomed-in image showing the printing sequence for one layer. After a layer is printed (green arrows), the printing moves inward (red arrow) and repeats for another layer (green arrows) until reaching the center. The resulting 3D structure is shown on the right. (E) A 3D AutoCAD model of a microlattice with octahedral unit cell. (F) Schematic of the compression testing apparatus for the AJ printed microlattice structures. (For interpretation of the references to color in this figure legend, the reader is referred to the web version of this article.)

printing system. The structures were built-up layer-by-layer from the stream of droplets exiting the nozzle and controlled by a shutter that diverted the droplet-flow as needed. The platen was heated to 90 °C to remove the solvents during printing process. As shown in Fig. 1D and E, a specific printing sequence gave rise to the 3D microlattice structures. The printed green structures were thermally sintered in a programmable oven (Neytech Vulcan furnace, Model 3–550, Degussa-Ney Dental Inc., Bloomfield, CT) at 350 °C for 2 h. The substrate used for printing was 10 mm × 10 mm × 2 mm polished and plasma pre-treated 96% pure alumina (ALN-101005S1, MTI Corp, Richmond, CA). The geometries of specimens were analyzed after sintering using a Scanning Electron Microscope (SEM, FEI Quanta 200F, FEI Inc, Hillsboro OR). The mass of the as-fabricated 3D microlattice scaffolds was obtained by comparing the mass of the substrate before printing and after sintering by an analytical balance (Radwag AS 60/220. R, RADWAG Inc, Miami FL).

### 2.3. Compression test apparatus

The AJ printed 3D microlattice structures were subjected to compression in a universal testing machine (Instron Inc., Norwood MA). High magnification video recording was done to provide additional information about the behavior of structures at the unit lattice scale and directly observe buckling and/or bending of the individual truss members. The custom-built test apparatus consisted of a fixture with a three-axis micro stage, a strain-based force transducer (EB7 subminiature load sensor, Loadstar Sensors, Fremont, CA), an optical magnifying tube (Infiniprobe TS-160, Infinity-USA, Boulder, CO), and two video recording cameras (Rebel T7i, Canon Inc, Tokyo, Japan). The arrangement is shown in Fig. 1E and Supporting Information, Fig. S1. A compression rate of 10 μm/s was applied during the tests (equivalent to a strain rate of  $7 \times 10^{-3} \text{ s}^{-1}$ ) to keep the process as close to quasi-static as possible [1,2,19]. The displacement measurement was verified independently using a triangulation laser displacement measurement apparatus (Keyence Inc, Itasca IL). This measurement was within 0.5% of that displayed by the Instron machine, indicating that the rigidity of the apparatus was high compared to that of the samples.

### 2.4. Compression modeling

The compression behavior of the printed microlattice structures was simulated by FEA using Nonlinear Explicit Code of the ABAQUS software (Dassault Systèmes Simulia Corporation, Providence RI). To simplify the simulations, 3D beam elements B32 (a 3-node shear flexible beam with quadratic interpolation) were employed to discretize the truss structures of the scaffolds as they best represent the physics of microlattice deformation; consistent with that in literature [34,42,43]. Note that a comparison of this 3D element with other possible elements is shown in the Supporting Information, Table-S1. The bottom and top plates of the apparatus are assigned as the discrete rigid elements to simulate the stationary substrate and the moving platen, respectively. All degrees of freedom of the lower plate were constrained and only one degree of freedom (up and down motion) was assigned to the top plate. The nodes of the scaffold at the connecting points with the bottom plate were fixed, while the top plate was made to move downward to compress the scaffold. For quasi-static simulation of scaffold structures, it is customary to achieve accurate results by reducing the time period of the analysis to millisecond range even when the tests are performed in

several minutes, especially for rate-independent materials (Refs. [16,44] and ABAQUS user guide), which was employed in this work.

## 3. Results and discussion

### 3.1. Design and fabrication of 3D cellular microlattice structures

Three different 3D microlattice structures were designed and fabricated in this work. Design considerations for the lattice structures included the target deformation behavior (stretching vs bending-dominated), and fabrication constraints such as the maximum overhang angle of 53° with the vertical while fabricating microscale freeform structures without any support materials [23]. It has been shown that stretching-dominated structures possess higher stiffness-to-weight ratio (defined as  $E/\rho$ ) while bending-dominated structures exhibit a relatively stable plateau stress region, representing high specific energy absorption [45]. In our study, the microlattice structures had unit cells having shapes of octahedral, hexagonal, and octahedral with central pillars which are all classified as bending-dominated. The octahedral structure with central pillars was designed to be deformed primarily by buckling (which is a subset of bending-dominated behavior) [28] when loaded along the pillar axis. Note that the bending-dominated structures exhibit a scaling relationship between Young's Modulus and strength as a function of density as,  $E/E_s \propto (\rho/\rho_s)^2$  and  $\sigma/\sigma_s \propto (\rho/\rho_s)^{3/2}$ , respectively, where  $E$  is the Young's Modulus,  $\sigma$  is the yield strength,  $\rho$  is the density, while the parameters with subscript 's' indicate the bulk values. Buckling-dominated structures have a buckling strength which is dependent upon elastic modulus rather than yield stress due to the buckling instability so the strength scales as  $\sigma/E_s \propto (\rho/\rho_s)^2$  [28]. In contrast, stretching-dominated structures exhibit linear scaling for both stiffness and strength [46].

The microlattice structures fabricated by the AJ printing process (Fig. 1) involved using a competition between surface forces and weight of the droplets coming out of the nozzle of the AJ printer (Fig. 1A and B). This process was completed without the use of any support material. The droplets containing nanoparticles and binders lose solvents as they reach the hot substrate which is at 90 °C (inset of Fig. 1B). Once the next droplet reaches the structure, it 'sticks' to the previously formed droplet rather than falling to the substrate due to surface forces. This process is exceedingly fast as the dispense of the mist of droplets is at an estimated speed of about a few meters per second and the flow of the mist can be interrupted at an accuracy of a few milliseconds (via a shutter – see Section 2). To account for the time lag between the shutter being able to stop the flow of the droplets and the stable formation of the circular truss member, the printing path for one ~20 μm layer on a truss is shown in Fig. 1C. This method of fabricating the truss members is repeated to construct 3D microlattice structures as shown in Fig. 1D. To allow sufficient time for the deposited droplets to be solidified, and also to keep printing consistent volume of the material in a printing layer, the printing path was designed per layer in a CAD program, with an example shown in Fig. 1D, where the arrows and arrow colors represent the printing sequence locally and globally, respectively. The printing sequence is programmed to progress to the next closest scaffold member to reduce the time to print a layer. The total print time is a function of the number of layers, type of geometry, and number of cells. For example, the lattices in this work are fabricated in approximately 0.5–2 h. Finally,

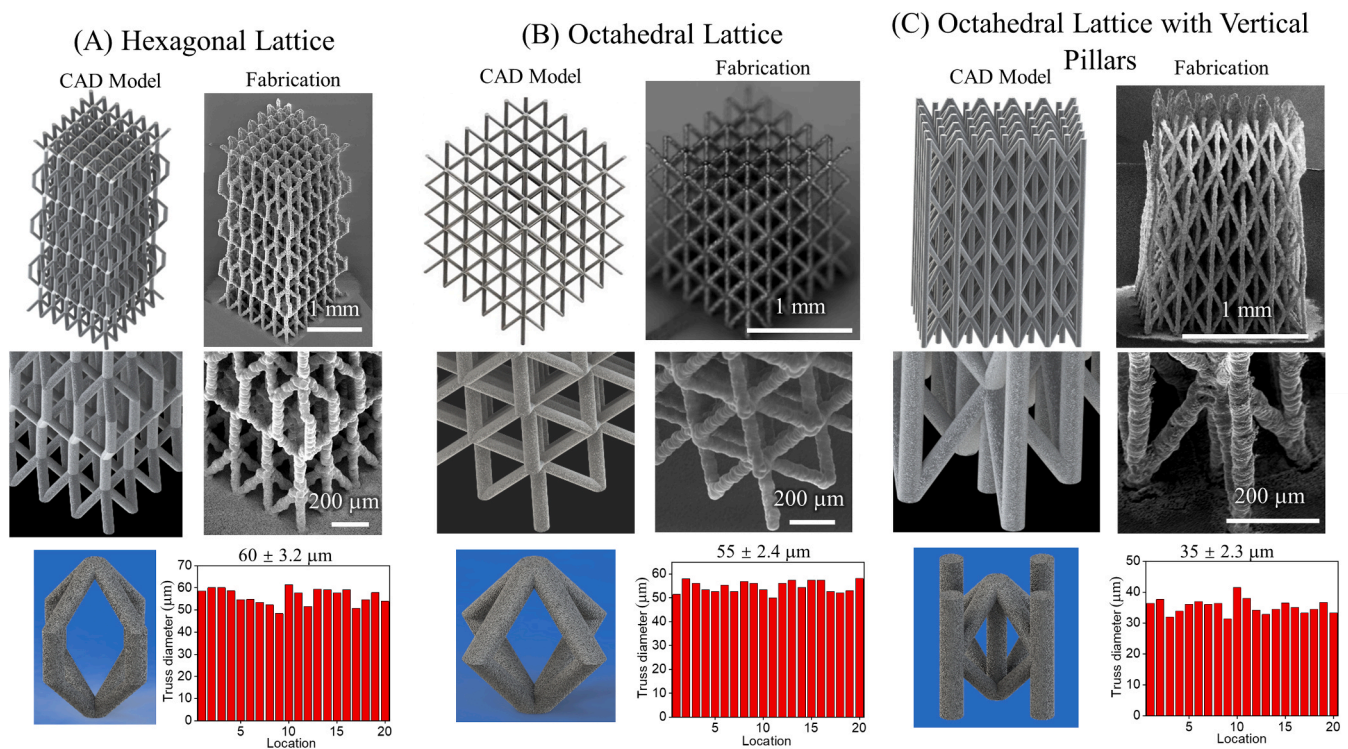
a microlattice structure is achieved by repeating this printing pattern until a desired height (layers) was reached. The geometry of a microlattice structure with octahedral unit cell is shown in the CAD drawing in Fig. 1E. After printing, the microlattices were heated to remove the binders and sinter the nanoparticles (see Section 2).

Fig. 2 shows representative 3D microlattice structures fabricated by the method described above with unit cells having hexagonal (Fig. 2A), octahedral (Fig. 2B), and octahedral with central pillar structures (Fig. 2C). The CAD drawings are also provided for comparison, including the unit cell structures (bottom) for each of the lattices. As seen in Fig. 2, the truss members of the microlattices have maintained their structure through the fabrication process. A close-up of the three printed structures is also shown in Fig. 2, along with the corresponding CAD images for comparison. The truss members show a signature of drop-by-drop additive assembly of the nanoparticles during the printing process. The truss diameters for each of the structures shown in Fig. 2 are within about 8% of the mean. We note that this variability is expected to increase when an entire lattice structure is built as more variables will be encountered during the printing process. For example, in case of lattices O-2, O-4 and O-8 with  $5 \times 5 \times 5$  structure (see Fig. S2 of Supporting Information and data in Table 1), we intended to fabricate structures with similar truss diameters and overall dimensions. The resulting truss diameters (Fig. S2) are within about 8% of the mean, but the overall dimensions are within 13% of the mean. In contrast, structures O-8 and O-9 exhibit considerably different overall dimensions (see Fig. S2 of the Supporting Information and data in Table 1). In this particular case, we intended to increase the truss diameter of O-9 compared to O-8 while maintaining the global density of the lattices. The former was achieved via a change in the printing program. To maintain the overall global density, the dimensions of O-9 lattice were increased via the printing program. Note that efforts to reduce the variability in the AJ printing process is an active area of current research [47,48]. Considering the manufacturing variability discussed above, the results shown in Fig. 2 clearly illustrate that true-to-design final structures are achievable with

the AJ printing method. Further, despite the variability, the lattice global density is the primary driver of the mechanical response of such structures as will be shown in Section 3.2.

As mentioned in the previous section, the diameter of the truss members could be tuned by varying the printing path and sheath gas/carrier gas pressure. Fig. 3A-C show the side view of three structures having different diameters obtained by changing the sheath gas/carrier gas pressures during printing. Note that the sheath gas/carrier gas pressures used in fabricating Fig. 3A-3C are 50/24, 46/27 and 50/25 (sccm), respectively (see Section 2). In addition, changing the radius of the printing path shown in Fig. 1C can also be used to change the truss diameter. This is illustrated in Fig. 3D, where three representative schematics of octahedral unit cells are shown with increasing radii of  $R_1$ ,  $R_2$  and  $R_3$ , which, with other printing parameters being kept the same, would result in increasing relative density. Note that for an  $R > 30 \mu\text{m}$  (or diameter of  $60 \mu\text{m}$ ), the deposited material left an inner 3D cavity with a radius of  $10 \mu\text{m}$  along the length of the truss member (bottom image of Fig. 3D).

Fig. 3D-right shows the SEM images capturing the change in truss diameter for the schematics in the Fig. 3D-left. Here,  $R_1$  is  $15 \mu\text{m}$ ,  $R_2$  is  $25 \mu\text{m}$  and  $R_3$  is  $40 \mu\text{m}$ . To reveal the unique hollow structure of  $R_3$  under SEM, certain parts of the outer shell of the hollow strut were removed by Focused Ion Beam (FIB) to expose the inner cavity as shown in Fig. 3E. Thus, the angle to take the image shown in Fig. 3D-right for  $R_3$  is different than  $R_1$  and  $R_2$ , this change was made to better expose the inner cavity. This image also shows the unique porous structure within the truss members due to sintering process of nanoparticles. The internal porosity due to sintering is about 15–20%. Note that the internal porosity is tunable by varying the sintering conditions [23,46], where increasing the sintering temperature from  $150^\circ\text{C}$  to  $550^\circ\text{C}$ , reduced the porosity from 50% to  $< 1\%$ . The SEM images as seen before and after the FIB etching in Fig. 3 reveal the capability of AJ printing to fabricate unique metallic microlattices with near-solid truss members with diameters of  $30\text{--}60 \mu\text{m}$  and unit sizes of  $100\text{--}400 \mu\text{m}$ . Table 2 shows the



**Fig. 2. CAD model and resulting microlattice structures via AJ printing.** (A) Microlattice with Hexagonal unit cell, (B) microlattice with octahedral unit cell, and (C) microlattice with octahedral unit cell with central pillars. The thickness of the truss members in each lattice were varied by changing the sheath gas pressure to achieve a certain volume fraction. The diameters of the truss members in a given microlattice are within  $\pm 8\%$  for all the three topologies considered in this work.

**Table 1**

Physical properties of 29 AJ-printed microlattice samples used in this study. Table contains geometric parameter gathered from SEM image (see SEM images given in Supporting Information, Fig. S2 for each sample). The mass measurements from analytical balance are used to calculate the relative density of each microlattice. The dimensional data from this Table was used in calculating the stress and strain for each sample during the compression tests. All samples were sintered in oven at 350 °C for 2 h.

Specimen Label	Length (μm)	Width (μm)	Height (μm)	Unit cell #	Volume (mm <sup>3</sup> )	Mass (mg)	Mass density (kg/m <sup>3</sup> )	Relative density
O-1	902	913	1605	5 × 5 × 4	1.32	1.11	836.9	9.98%
O-2	939	935	1644	5 × 5 × 5	1.44	1.15	794.9	9.48%
O-3	968	1021	1769	5 × 5 × 8	1.75	2.55	1456.3	17.35%
O-4	988	1008	1635	5 × 5 × 5	1.63	1.67	1028.6	12.26%
O-5	1274	1255	1769	8 × 8 × 4	2.83	3.12	1102.2	13.14%
O-6	1578	1555	1950	5 × 5 × 4	4.78	2.68	561.0	6.69%
O-7	1967	1975	1157	5 × 5 × 4	4.49	2.22	493.9	5.89%
O-8	873	863	1343	5 × 5 × 5	1.01	1.17	1155.5	13.78%
O-9	1243	1224	1828	5 × 5 × 5	2.78	2.46	883.7	10.53%
O-10	1008	1012	963	5 × 5 × 4	0.98	1.22	1241.4	14.79%
O-11	2714	2786	1563	8 × 8 × 4	11.82	10.22	864.8	10.30%
O-12	1761	1769	1673	10 × 10 × 10	5.21	11.44	2195.0	26.16%
O-13	1555	1504	1390	5 × 5 × 5	3.25	2.39	733.8	8.75%
O-14	1333	1355	1504	6 × 6 × 6	2.72	2.40	884.8	10.55%
O-15	911	923	1680	5 × 5 × 4	1.41	1.82	1286.0	15.33%
VP-1	1001	1015	1345	4 × 4 × 3	1.37	0.77	561.5	6.69%
VP-2	991	1017	1368	4 × 4 × 4	1.38	1.19	864.3	10.30%
VP-3	971	941	1426	3 × 3 × 3	1.30	0.71	542.1	6.46%
VP-4	1250	1257	1200	4 × 4 × 4	1.89	2.47	1309.1	15.60%
VP-5	981	990	1420	5 × 5 × 4	1.38	2.81	2036.0	24.26%
HX-1	1649	1649	1390	6 × 6 × 3	3.78	1.71	451.4	5.38%
HX-2	1709	1709	1595	6 × 6 × 3	4.66	2.75	590.8	7.04%
HX-3	1705	1705	1900	6 × 6 × 3	5.52	2.88	522.0	6.23%
HX-4	1759	1759	1539	6 × 6 × 2	4.76	4.37	917.0	10.93%
HX-5	1733	1733	1461	6 × 6 × 3	4.39	3.74	851.8	10.15%
HX-6	1745	1745	745	6 × 6 × 1	2.27	1.93	851.5	10.15%
HX-7	1152	1152	957	5 × 5 × 1	1.27	0.61	480.3	5.73%
HX-8	913	913	2266	5 × 5 × 3	1.89	1.27	672.4	8.01%
HX-9	1063	1079	1578	5 × 5 × 3	1.81	0.90	497.7	5.93%

uniqueness of our approach in comparison with other advanced manufacturing techniques used to fabricate three-dimensional microlattice structures.

Before compression tests, all samples were imaged under SEM and weighed to measure the geometrical parameters, and identify physical properties, and local defects. This data for 29 three-dimensional microlattice structures fabricated in this study are shown in Table 1 and the corresponding SEM images, dimensions, and densities are included in Supporting Information, Fig. S2.

### 3.2. Compression behavior of the scaffold structures

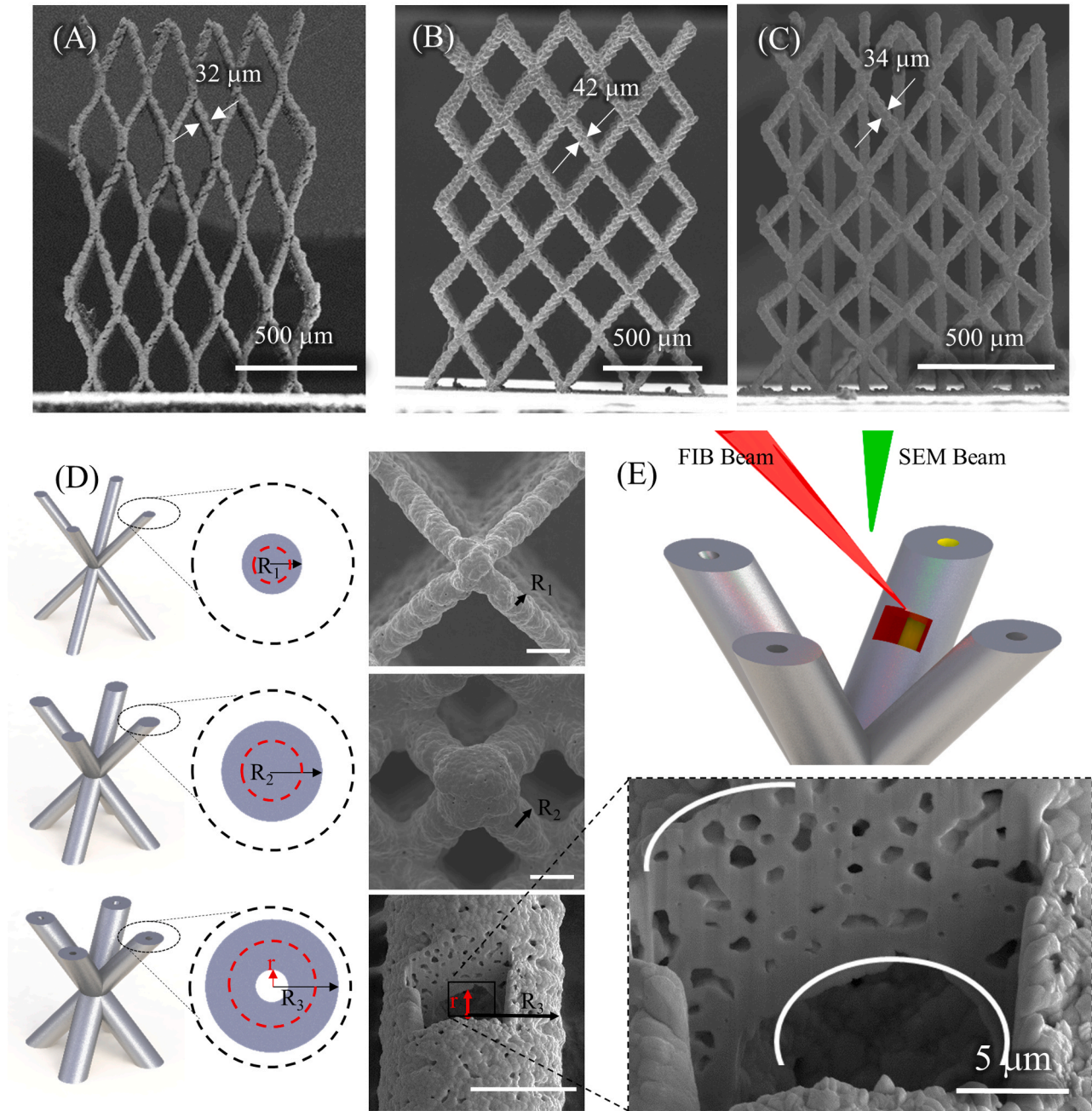
#### 3.2.1. Experimental results

Fig. 4 shows the optical images and stress-strain behavior of four microlattice geometries having octahedral unit cells without (Fig. 4A and B) and with (Fig. 4C and D) vertical pillars. The octahedral structures without the pillars have a relative density of 7.6% (sample O-2) and 11% (sample O-8) and are shown in Fig. 4A. Their engineering stress as a function of engineering strain is shown in Fig. 4B. Note that while plotting Fig. 4B, the force-displacement data recorded during the test was converted into engineering stress and engineering strain by taking the ‘overall’ cross section area (length multiplied by width) of the microlattice and the initial microlattice height (Fig. S2 of the Supporting Information shows SEM images and length, width, and height measurements as measured under an SEM for all the 29 lattices used in this study). In addition to the stress-strain plot, the images captured from compression video at different strain levels are also included in Fig. 4B. The stress-strain relationship showed an initial linear region up to a strain of about 5–7%, followed by a long plateau until a strain of about 60%, after which the densification regime started to dominate. This behavior is qualitatively similar to that for macroscale scaffolds [30]. In the linear region, all the unit cells responded to the compression loading uniformly as stresses were distributed almost instantaneously due to the lack instabilities such as buckling or large bending deformation. The

effective Young’s Moduli of the microlattice samples O-2 and O-8 were 9.7 MPa and 11.2 MPa, respectively.

As the stress increased in Fig. 4B, the deformation of the microlattice structures became nonlinear (in the stress plateau region). This process was initiated due to local deformation/stress concentration at some ‘weak’ unit cells. Such cells are circled in the images shown in Fig. 4B, where they underwent bending/collapse first. The plateau region is thus a result of bending-driven collapse of one or more truss members in the microlattice, while the drop in the stress is attributed to failure of unit cells including truss members and the connecting nodes. The plateau stress for the octahedral lattice with 7.6% density was about 50% lower than that with a density of 11% and this relationship will be further discussed later in this section. Within the plateau region, the initial collapse propagated to form a ‘band’ within the lattice. The global engineering stress started to rise again for the two structures at a strain of 26% and 32%, primarily due to the full collapse of the first batch of the ‘weaker’ cellular units as their adjacent trusses start to touch each other. This periodic hardening and softening is repeated through the plateau region, but the oscillations are within 10% of the nominal plateau stress for the octahedral structures. When most of the cells collapsed, the global stress-strain relationship went into the third, densification, region at a strain > 60%. In this region, the stresses increased dramatically as all the unit cells had collapsed and the entire microlattice structure was compacted.

The slope of the elastic region and the oscillations in the plateau region could be changed/tuned by introducing pillars into each unit cell as shown in Fig. 4C (also see Fig. 2C). This is a result of the fact that vertical pillars suppress bending and shift the dominant deformation mechanism to buckling of the individual members. Thus, the compression of the scaffold was controlled by the buckling instability rather than (a stable) bending. We expect the vertical pillars to increase the effective modulus of the stress-strain response as the pillars are in direct compression rather than bending. Two microlattices with vertical pillars fabricated by AJ printing, VP-2 (relative density of 8.2%) and VP-3



**Fig. 3. Microscopic characterization of sintered microlattices.** (A) SEM image of a  $5 \times 5 \times 3$  microlattice with hexagonal unit cells, (B) SEM image of a  $4 \times 4 \times 4$  microlattice with hexagonal topology, and (C) SEM image of a  $4 \times 4 \times 4$  microlattice with octahedral unit cells with vertical pillars. The truss diameter and relative density ( $\sigma/\sigma_s$ ) could be varied for these structures. (D) Representative octahedral unit cells with different strut radii and their microscopic characterization along with the printing path (red dotted line). (E) A schematic and a SEM image showing certain parts of outer shell of a hollow strut etched by FIB. Scale bars in (D) represent  $50 \mu\text{m}$ . (For interpretation of the references to color in this figure legend, the reader is referred to the web version of this article.)

(relative density of 5.2%), are shown in Fig. 4C. The engineering stress – engineering strain curve along with images of the microlattice with vertical pillars at various strain levels during the compression test are shown in Fig. 4D. As expected, for  $< 5\%$  strain, the response of the scaffold was linear with slopes higher than that observed for octahedral structures when structural density is taken into account. However, the major change was observed in the plateau region. As the stress reached the plateau region, a sudden drop in stress could be observed. This is attributed to the simultaneous buckling of the vertical members across an entire horizontal layer. Thus, the buckling mode of deformation localizes the failure to a single layer at a time. This was followed by a sharp increase in stress until a second stress drops occurred at 25% (VP-2) and

28% (VP-3) strain. This effect was caused by bulking of second layer of the unit cells. The microlattices VP-3 and VP-2 showed three and four significant stress peaks corresponding to their 3-layer and 4-layer structures, respectively. The stress oscillations in the plateau region in Fig. 4D are as high as 35% of the nominal plateau stress. Once the densification regime was reached at around 60–65% strain, the stress increased significantly in accordance with the expected densification. The engineering stress – engineering strain response for hexagonal microlattice structure is largely similar to that for the octahedral structure and can be seen in Supporting Information Fig. S2.

The results in Fig. 4 show that AJ 3D printing can create metallic microlattice structures with near-solid truss members that can be tuned

**Table 2**

Comparison of different manufacturing techniques for the fabrication of three-dimensional microlattice structures.

Microscale 3D Printing techniques for nano/micro lattices	2D feature accuracy	Smallest 3D feature	Type of structure	Comment
Freeform printing [10–12]	< 10 $\mu\text{m}$	20 $\mu\text{m}$	Spatial interconnects	1) Non-intersecting features (i.e., cannot construct complex 3-D scaffold structures) 2) Nanoparticles dispersed in viscoelastic inks, leading to a significant portion of the structure being the matrix/binders between the particles
Polymer Templating followed by metal or ceramic coating to get 3-D structures with hollow truss members [10,19,20]	NA	< 1 $\mu\text{m}$ if 2-photon lithography, $\sim 10 \mu\text{m}$ for other templates	Lattices	1) Final metal/ceramic product consists of intricate lattices with hollow tubes (not fully dense truss elements). 2) Requires the use of chemicals to dissolve the template and added step to manufacturing 3) Hierarchical features/structures as shown in Fig. 2 have not been demonstrated.
Inkjet Printing (Refs. [13–15])	$\sim 60 \mu\text{m}$	$\sim 100 \mu\text{m}$	Micro-wires and Pillars	1) Low accuracy over the structural features and hence demonstration of simple micro-wires only 2) Length scales related to sintering and lacks structural hierarchy shown in Fig. 2
Current work: AJ printed three-dimensional microlattices	10 $\mu\text{m}$	20 $\mu\text{m}$	Micro-lattices	1) Near fully dense truss members (porosity < 20% and can be further reduced by changing the sintering conditions) forming complex 3-D architectures 2) Use of Aerosol Jet creates finer features compared to other solution based noncontact processes 3) Noncontact method allowing higher structural complexity 4) Mechanical properties can be tuned via changing the printing parameters and designs. 5) Can potentially use a variety of feedstock materials such as metals, ceramics, metal oxides, and polymers, along with their mixtures.

to mechanically deform via different mechanisms. The behavior of the lattices in Fig. 4B and Fig. 4D are due to bending-driven deformation, and buckling-driven collapse of the lattice, respectively. Although the two structures showed a similarly long stress-plateau region, the introduction of vertical pillars in Fig. 4D increased the stiffness and localizes the deformation to a single layer at a given time; with other layers remaining largely intact, until they underwent buckling as well. The vertical pillars also amplified periodic hardening and softening in the plateau region primarily due to the fact that buckling is an instability driven by statistics rather than being a deterministic failure mode.

### 3.2.2. Modulus and yield strength as a function of relative density

We now look at the relative stiffness and compression strength of the three types of microlattice structures as a function of the relative density. While plotting this data, the elastic modulus of the sintered porous silver ( $E_s$ ) was taken to be 1500 MPa from our earlier work (Saleh et al. [46]). For silver structures sintered at 350 °C, the elastic modulus was reported to be about 1500 MPa, which changed to 2300 MPa for a sintering condition of 250 °C. Another paper measured the elastic modulus of Ag nanoparticles sintered at 380 °C via nano-indenter and reported a value of 4600 MPa [49]. Since there is some variation in this data, we chose 1500 MPa as the elastic modulus,  $E_s$ , of the sintered porous silver because the sintering and testing conditions in Ref. [46] more closely matched the conditions reported in this work. The yield stress of the porous silver,  $\sigma_s$ , was determined to be 45 MPa for a porosity of about 20% [46].

Fig. 5A shows the elastic modulus of the octahedral microlattices with and without central pillars, as well as the hexagonal microlattices. The modulus data closely followed quadratic scaling as a function of density as expected for bending-dominated structures as described in Section 3.2.1. However, the behavior of the structures with pillars displayed buckling-dominated behavior resulting in a larger relative stiffness for a given lattice density when compared to the octahedral lattice structures. The hexagonal structures, however, have some deviations, possibly due to the variation in the printed structures. Table S2 of Supporting Information shows the scaling factors of the microlattices. Fig. 5B shows the relative compressive strength as a function of density for the microlattice structures. The strength of all the structures scaled as

that for bending-dominated structures with a slight deviation for the octahedral structures with vertical pillars. The compressive strength of bending-dominated lattices is expected to scale according to Ashby model [28] as  $\sigma/\sigma_s \propto (\rho/\rho_s)^{3/2}$ . However, Ashby also described strength dominated by buckling failure, which is a subset of bending-dominated behavior. Euler buckling load is invoked in this model, which is a function of the stiffness of the material, and the scaled strength is then normalized by the modulus which is expected to be proportional to the square of the relative density. The best fit of the octahedral structures with central pillars had an exponent of 1.42 when scaled with the compressive strength, indicating a less severe reduction in compressive strength relative to the octahedral and hexagonal structures. This is likely due to the anisotropic nature of the structure which has continuous pillars along only one axis. Instead of deforming as an isotropic lattice failing by elastic buckling as described by Ashby [28], the presence of pillars here was able to support direct compressive loads along the entire length of the structure, resulting in a higher stiffness and strength along that direction. On an average, the strength and yield stress of the octahedral structures without the central pillars is lower than that with the central pillars. Thus, AJ printing, a microscale 3D printing process, can create structures with microscale lattice elements with tunable properties within the expected range of values. Note that the overall range of relative density is from 5.4% to 26.2%, the relative stiffness is in the range of 0.1% to 6.3% and the relative strength is ranged from 0.2% to 9.0%, respectively.

Based on the SEM images of the 29 scaffolds tested in this work (Fig. S2, Supporting Information), we note that several scaffold structures printed in this work have defects, a fact that is common to almost all the 3D printing processes. These defects include non-uniformity in the sizes of the unit cells, macroscopic cracks in the lattice, and cracks/breaks within the truss structures. In addition, we see the corrugated structure for the truss members (Figs. 2 and 3), which is a direct result of the manufacturing process described in Section 2.2. Note that there is a significant scatter in the relative stiffness (Fig. 5A) and relative strength (Fig. 5B) for microlattices with hexagonal geometry. This may be a result of random defects in AM sintered nanoparticle structures which could also be observed in octahedral lattices and octahedral lattices with vertical pillars. However, large defects can be found in samples HX-6

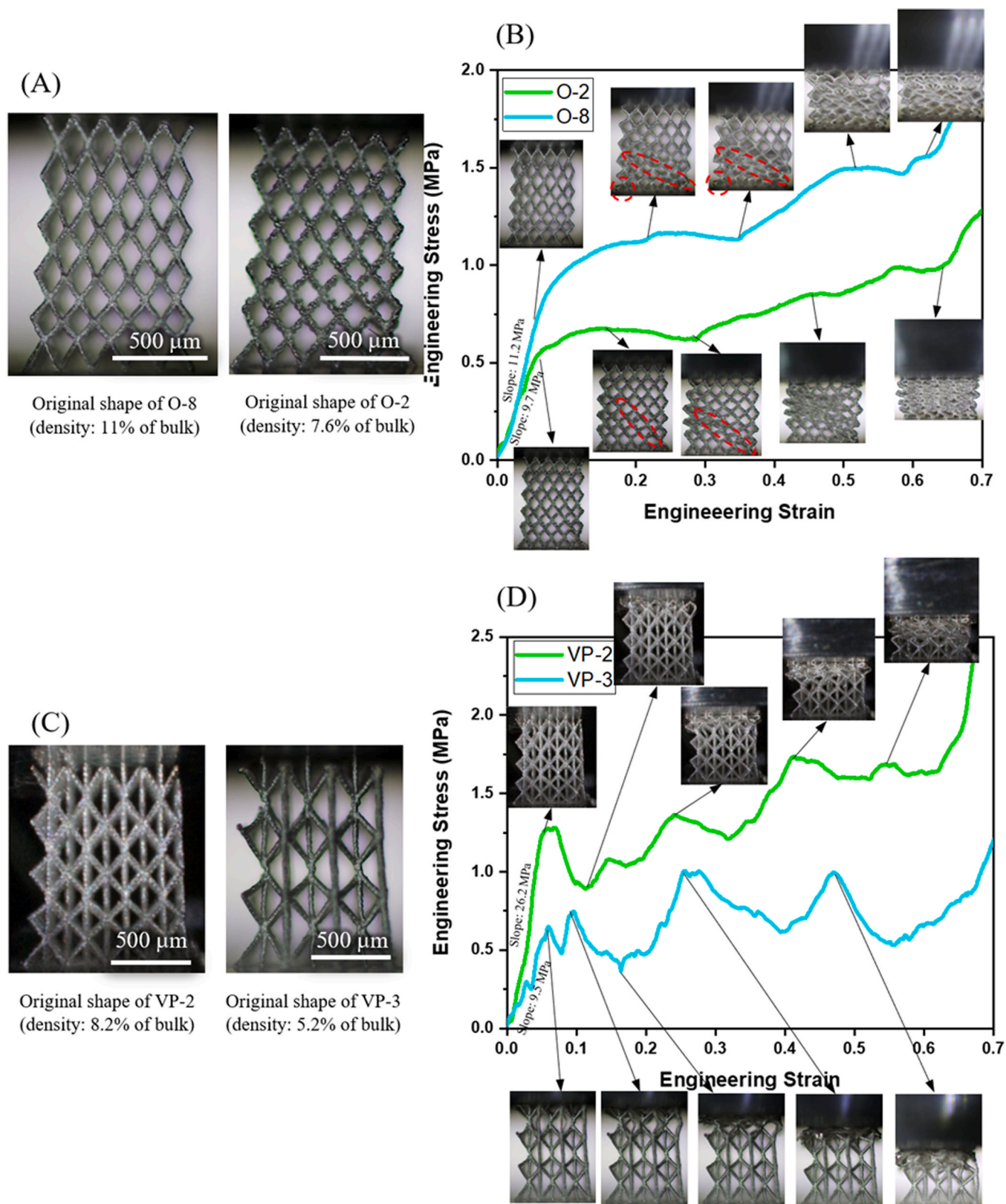
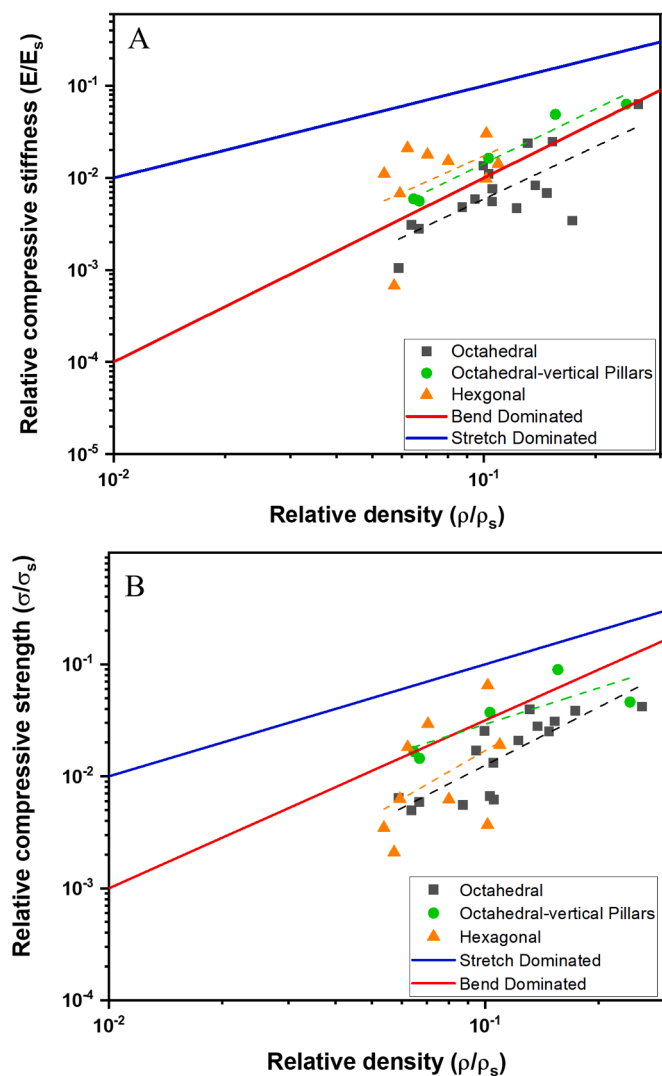


Fig. 4. Comparison of the mechanical response of different AJ printed microlattice structures. (A) Original shape of two octahedral samples and (B) their stress vs strain plots under uniaxial compression loading. (C) Original shape of two octahedral samples with central pillars and (D) their stress vs strain plots under uniaxial compression loading.



**Fig. 5.** Relative stiffness and compression strength of AJ printed microlattice structures as a function of their relative density. Data from uniaxial compression tests showing (A) relative stiffness vs relative mass density and (B) relative plateau stress vs relative mass density for the AJ printed microlattice structures. Lines representing linear scaling of stretch-dominated structures and quadratic scaling of bend-dominated structures are also included for comparison.

and HX-7, while samples HX-1, HX-2, HX-4 and HX-5 are rather uniform (see SEM images in Fig. S2). These variations could contribute to the significant scatter for this particular geometry. As seen in Fig. 5A and Fig. 5B, however, the global stress-strain response of microlattice structures does follow the prediction of a standard bend-dominated mechanism. We note that it is experimentally impossible to fabricate microlattices with identical densities because of the randomness of defects and manufacturing limitations. However, microlattices within a certain range of relative densities (from 6% to 10%) can be fabricated as shown in this work. The results in Figs. 1, 2, and 5 show that for mechanical deformation under compression, the structures have a significant tolerance to manufacturing defects. This is important from fabrication perspective as fast fabrication of 3D printed structures can lower the cost of manufacture, which is highly important from application perspective.

Silver was chosen to construct the microlattice structures in this work due to its prior usage in AJ printing [23–25,46,50,51] as well as its relative ease of sintering at low temperatures [41]. We note, however, that since AJ printing uses a mist of droplets (each containing

nanoparticles of the material of interest) to construct the structures, 3D microlattices can be fabricated from any material using this method. In fact, in our recent work, AJ printed 3D gold structures have been fabricated and used for sensing of COVID-19 antibodies [52]. We have also demonstrated 3D structures of acrylated-urethane polymers for use as dielectrics in antenna applications [24]. The AJ printing of complex 3D structures of metal oxides, 2D materials such as MXene, and additional polymers and metals without any support structures will be part of a future investigation.

### 3.3. Numerical prediction of compressive behavior

The deformation behavior of the three types of scaffold structures was shown to depend upon the microlattice design as discussed in Figs. 4 and 5. Although the experimental data (Table 1 and Fig. 5) can allow us to understand the mechanical behavior of the microlattices, computational and/or theoretical models can provide an excellent means of predicting their behavior for a multitude of shapes and sizes. A finite element analysis was thus performed to capture the compression behavior of the scaffold structures. Fig. 6A shows the model set-up to capture the microlattice stress-strain behavior using FEA (also see Methods section for the details of the model). A mesh convergence study was performed to ensure an adequately fine mesh for stable results (Supporting Information, Fig. S3). The material properties discussed in Section 3.2.2 were used for the ABAQUS FEA model. Due to the large strain effects that were modeled, non-linear material properties were utilized, and the tangent modulus was estimated to be 10% of the elastic modulus.

#### 3.3.1. Size effects

First, we note that the scaffold structures studied in this research have an  $n \times n \times n$  unit cells in the lattice, with  $n$  being 3–10 (see Table 1). In real applications, however, we expect to have large  $n$  values. It is thus imperative to see if any size effects exist in the observed compression behavior of the microlattices. It has been reported that lattice structures with finite size behave differently than lattice structures with large number of unit cells, and a support of the outer edges of the lattice stiffens the structure [53]. For our printed samples with octahedral topology, the outer edges in our structures do not have additional supports. However, as the number of unit cells increases, the added outer unit cells start to act as supports or constraints to the inner unit cells that may cause the mechanical properties of the microlattice to change with the structure.

We studied the lattice size effect by carrying out FEA study on six scaffold structures with  $1 \times 1 \times 1$ – $12 \times 12 \times 12$ -unit cells as shown in Fig. 6B. The reason  $n$  was chosen from 1–12 was based on our experiments where  $n$  was from 3 to 10 and the most were ranged from 4 to 6. Potentially we could conduct the FEA with larger number of unit cells, but we believe the size effects are small enough to be neglected in a range that fully covers our experiments. Identical unit cell sizes were used for comparison for all the lattices. Fig. 6C shows the engineering stress-engineering strain relations of all the six scaffold structures. As the number of unit cells increased, the stress-strain relation tended to be more ‘stable’ in the plateau region. This effect could be attributed to number of interior cells (supported on all sides by neighboring cells) increasing more rapidly than the number of exterior cells. Effective Young’s Moduli and plateau stresses of these structures are shown in Fig. 6D, representing the stiffness and strength of lattice structures. Despite the discrepancy of sample  $1 \times 1 \times 1$ , the other samples ranging from  $2 \times 2 \times 2$ – $12 \times 12 \times 12$  hold stiffness and strength within 9% and 7%, respectively. This variation is even smaller for scaffolds with  $4 \times 4 \times 4$ – $8 \times 8 \times 8$ -unit cells (1.5% and 2.6%) where most of our printed lattices reside (Table 1). When compared with the stiffness and strength differences caused by the changing of relative densities, these effects are small enough to be neglected and we conclude that size effects have only a marginal impact on the mechanical response of the

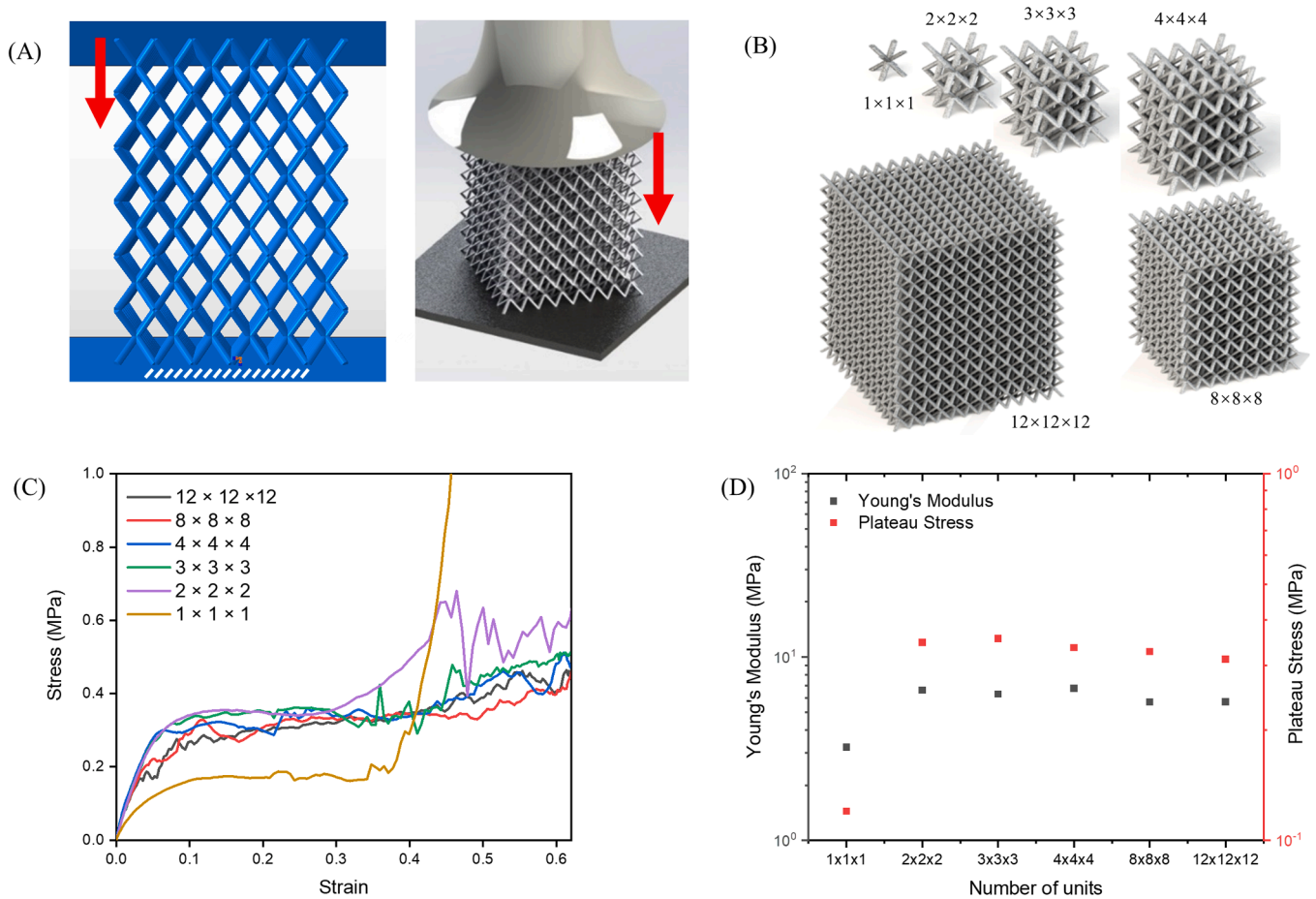


**Fig. 6.** Finite Element modeling of octahedral lattices. (A) FE model of a lattice with constraints and loadings (left) and schematic of the compression test (right). (B) Schematics of FE models of lattices with different numbers of identical unit cells (from  $1 \times 1 \times 1$  to  $12 \times 12 \times 12$ ). (C) Stress vs strain plots by FE modeling for the lattices in (B). (D) The Young's modulus and plateau stress for the data in (C).

samples in our study.

### 3.3.2. Comparison with experiments

We now compare the FEA models with corresponding experimental observations. Fig. 7A shows the experimental stress-strain response and the FEA prediction for compression of a representative sample (O-9 of Table-1). The FEA predicts a Young's Modulus of 10.0 MPa, which is within 3.1% of that observed in the experiment (9.7 MPa). The plateau stress predicted by the FEA is 0.51 MPa, vs the experimental value of 0.44 MPa, representing a difference of 15.9%. The FEA also captures various features of the stress-strain response in three regions, i.e., elastic, plateau, and densification regions. By taking the manufacturing defects and testing errors that may cause the variations of experimental results into account, the FEA predictions show a match with the experimental results.

A detailed frame by frame comparison of videos recorded from compression tests vs. the deformation predicted by FEA provides more evidence of the capability of the model to capture the structural deformation of the microlattices (Fig. 7B). The deformation of the entire lattice structure in FEA is symmetric about the vertical planes through the center, but not to the horizontal plane. The deformation in experiments is not as symmetric as shown by the FEA model due to imperfections in fabrication processes, yet significant details are captured by the FEA model as shown in Fig. 7B. When compression starts, the entire lattice responds elastically until Point-1 ( $\epsilon = 4.9\%$ ), when the localization of the stress occurs. Stress is most localized at the connection points in the top members due to the lower connectivity of those members and consequently lower resistance to bending. The central members of the

scaffold then become supported by the bottom end which is fixed to the supporting plate providing fewer degrees of freedom and stiffer behavior. This behavior is qualitatively similar to that observed in experiments as seen at Point-2 ( $\epsilon = 10.9\%$ ), where the red rectangle shows the deformation at the top end, which is much larger than the rest of the scaffold (especially at the bottom). The red circle at Point-2 indicates deformation of an individual cell near the center, where the strain is locally elevated. At about 15.3% strain, the stress is in the plateau region and more unit cells around the central part of the scaffold are influenced by the elevated localized strain. This results in the localized bending and yielding. The shape of unit cell that was circled at Point-2 is further distorted at Point-3, indicating that this point acted as a 'source' for the deformation in the central area of the scaffold at Point-3. Note that there is a small stress drop after Point-2 which might be explained by the simultaneous collapse of several members in the top layer of unit cells. At Point-4 in Fig. 7B, the central and top rows of cells have collapsed at a strain of about 33%, a process which influences and destabilizes the neighboring rows. Differences between experiments and FEA can be seen at this stage as some asymmetry with respect to vertical axis is observed in the experiments that may be due to some imperfections of the scaffold itself. This asymmetry, however, cannot be captured in the FEA simulations, but does not appear to significantly affect the stress-strain response. As the strain increased, more cells collapsed, and the slope of the stress-strain relation began to increase due to densification. At Point-5, all the unit cells have collapsed as seen in the experiment (also captured by the FEA model). A stress oscillation was noticed for strain in range of 40–60% due to the periodic collapse of the bands of unit cells. At Point-6 where strain is 67%, all cells collapsed further,

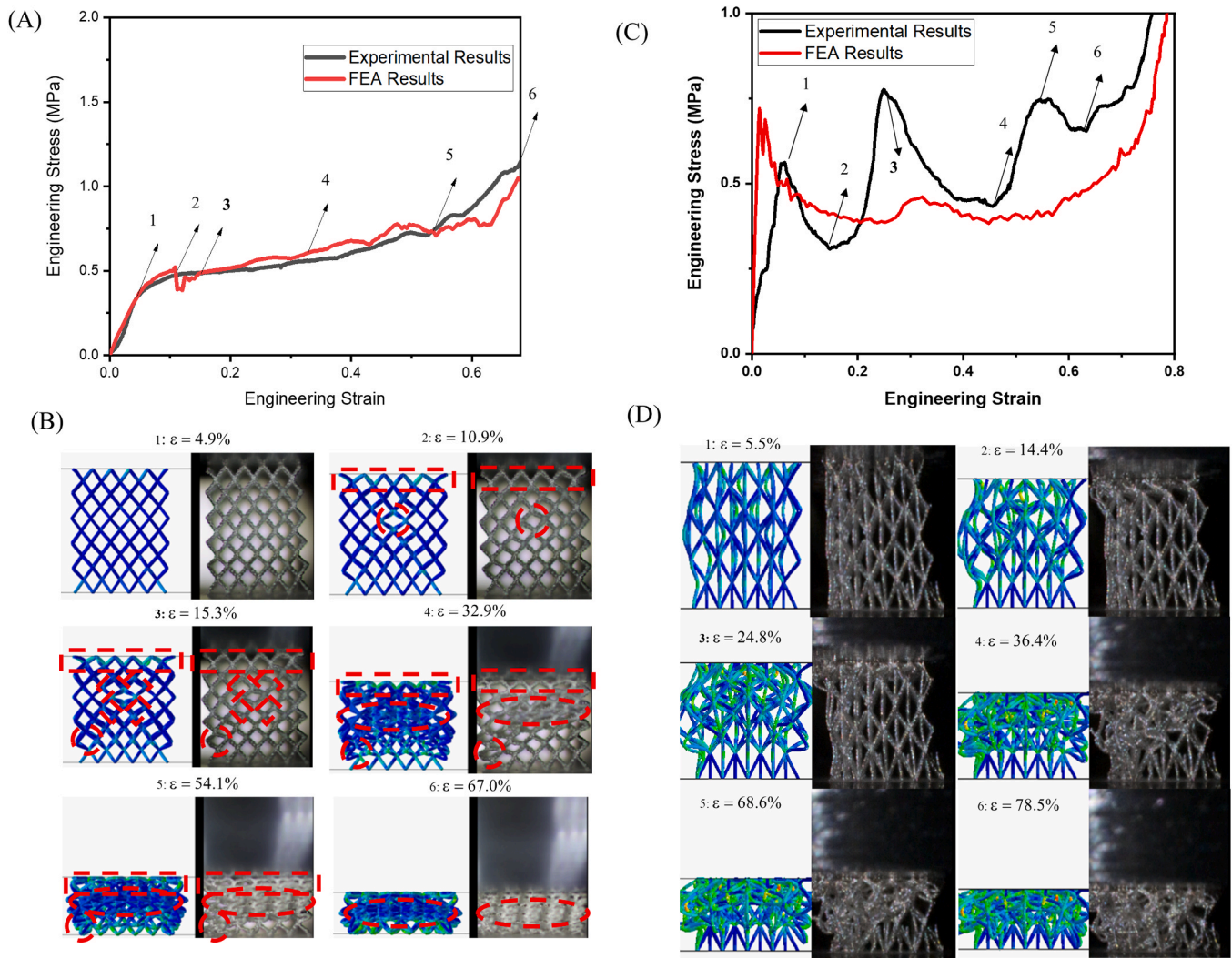


**Fig. 7. Comparison of mechanical properties between FEA predictions and experimental observations.** (A) Comparison of the global stress-strain response predicted by the FEA model and the experiments for an octahedral microlattice structure under uniaxial compressive loading. (B) A detailed frame-by-frame comparisons of FEA with experimental results showing deformation, bending, and collapse in localized truss members and unit cells. Dashed boxes, ellipses, and circles indicate localized regions that are visually compared. (C) Comparison of the global stress-strain response predicted by the FEA model and the experiments for an octahedral microlattice structure with central pillars under uniaxial compressive loading, and (D) a detailed frame-by-frame visualization of the data in (C). Since the failure in (C, D) is governed by buckling, an instability, the FEA cannot capture the strong oscillations in the stress-plateau region. Also, the defects introduced by additive manufacturing lead to a layer-by-layer failure of the microlattice, which is not captured by FEA which predicts a more uniform collapse.

resulting in compaction of the structure in both FEA and experiments. The video of the collapse of the micro-scaffold in the experiment and that predicted by FEA is shown in Supporting Information Video S1. We thus conclude that the FEA model was able to capture the compression behavior of the octahedral structure, which represents bending-dominated deformation.

We then carried out FEA of octahedral structures with central pillars under compression and compared these results with the experimental observations (e.g. Fig. 4C and D). These results are summarized in Fig. 7C and D. Also see the video of the comparison of the two in Supporting Information, Video S2. It is clear from Fig. 7A that the FEA can only partially capture the compression behavior of the scaffolds where the collapse is controlled by buckling, which is an instability. The frame-by-frame comparison shows that the collapse of the microlattice happens layer-by-layer as described before. The FEA, however, captures the vertical columns as single elements through the thickness and a more uniform collapse of the structure is predicted. A prediction of uniform collapse cannot capture the strong oscillations in the stress plateau region of the stress-strain plots seen in experiments.

We thus conclude that FEA can indeed capture the compression behavior of the microlattices that show bending-dominated deformation but cannot do the same for the structures where deformation involves significant buckling. In any foam-like structure with irregular microstructure and ligaments, some degree of deformation will be controlled by local buckling and thus simple FEA models will not be sufficient to capture their deformation. New modeling efforts are thus needed for cellular materials, where local effects caused by stress/strain gradients and defects need to be taken into account [54] and will be part of a future investigation.

Next, we ran the FEA simulations for all the octahedral samples shown in Table-1 and compared the predicted stiffness and yield strength with respect to that observed in the experiments as shown in Fig. 8. The FEA models were based on the sample dimensions measured under SEM (Fig. S2). Note that the model densities were slightly different compared to that measured by mass density of the samples. This difference, however, was small enough to be negligible as shown in Supporting Information, Table S3. As seen in Fig. 8A, the relative compressive stiffness ( $E/E_5$ ) as a function of the relative density as

predicted by the FEA model is quite similar to that predicted by the experiments. In particular, the FEA results show a slightly lower scaling factor (i.e., slope) of 1.73 vs. 1.91 seen in experiments, which follows the expected bending-dominated behavior of  $(E/E_s)\propto(\rho/\rho_s)^2$  described by Ashby's model [28]. Fig. 8B shows the relative compressive strength as a function of the relative density, again exhibiting common ideal bending-dominated behavior with  $(\sigma/\sigma_s)\propto(\rho/\rho_s)^{3/2}$  with the FEA scaling factor being 1.84 vs that for experiments of 1.45. These results show that the FEA model proposed in this paper can capture and predict the mechanical properties of 3D microlattice structures.

### 3.4. Theoretical model to predict compressive behavior

The bending-dominated cellular structures discussed in this work have excellent energy absorption characteristics and consequently several phenomenological models have been proposed to help predict their stress-strain behavior under uniaxial compression. These models are semi-empirical and are based on fitting of the experimental data to the models [35–40]. These models [35–40], however, have been developed for random foams rather than ordered lattice structures studied in this work and are incapable of predicting the periodic

hardening and softening behavior observed in the stress plateau region shown in this study (Figs. 4 and 7). We note that Rusch [35] first introduced a simple model with only two terms, that - despite its simplicity - effectively captured stress-strain relations, especially in the densification region. Recently, by combining and modifying previous models, Avallé et al. [55] proposed a model for foam materials that contains three terms that can capture the stress-strain relation in the elastic region, the plastic region, and the densification region. This model is defined as,

$$\sigma(\varepsilon) = \sigma_p[1 - \exp(-m\varepsilon)] + \sigma_s\varepsilon + \sigma_D\varepsilon^n, \quad (1)$$

where  $\sigma_p$  is the plateau stress,  $\sigma_s$  is the linear hardening slope,  $\sigma_D$  is the Rusch densification parameter,  $m$  is the linear-plateau transition constant, and  $n$  is the Rusch densification exponent. The model, however, lacks the ability to capture the periodic softening and hardening (i.e., oscillating) behavior of the ordered lattice structure that is composed of multiple unit cells.

In order to bridge this gap, we propose a model that captures all the features of the stress-strain behavior observed in this work (Figs. 4 and 7). This is done by introducing an extra term into Eq. (1) that represents the stress plateau region. This term is:  $\sigma_s\varepsilon[1 + A\cos(f\varepsilon^u)]$ , which modifies the model in Eq. (1) to:

$$\sigma(\varepsilon) = \sigma_p[1 - \exp(-m\varepsilon)] + \sigma_s\varepsilon[1 + A\cos(f\varepsilon^u)] + \sigma_D\varepsilon^n, \quad (2)$$

where  $A$  is the oscillation amplitude,  $f$  is the oscillation frequency, and  $u$  is the oscillation delay.

In a uniaxial compression test, the oscillating behavior does not occur directly after the elastic region and increases in amplitude as strain increases which is the reason the new term is introduced with the existing  $\sigma_s\varepsilon$  term. However, the oscillations seen in the stress-strain plots are only in the stress-plateau region. To ensure this delay, an exponent to the strain has been added inside of the cosine. This causes the beginning of the oscillations to be at a low frequency at low strains which delays the impact of this term until the stress-plateau region is reached. However, it must be balanced so that the oscillations do not become too frequent near the densification region. The  $f$  term is a frequency term to scale the strain to an appropriate frequency. Fig. 9 shows the proposed model fit to experimental data, and the contribution of the additional term to the existing model. The additional term is demonstrated to effectively capture the periodic stiffening and softening of the structures, which extends the capability of the model to determine mechanical response in the plateau region of the microlattices. Five octahedral samples with similar unit cell structures ( $5 \times 5 \times 5$ ) were fit with the new model to investigate whether the model could be used to predict behavior of similar structures. The model parameters for this sample set were determined to be  $0.23 \pm 0.06$ ,  $26 \pm 2$ , and  $1.7 \pm 0.2$  for parameters  $A$ ,  $f$ , and  $u$ , respectively, showing close agreement. The details of the model fit can be found in Table S4 of Supporting Information. Although the additional term to the model in Eq. (2) is phenomenological, it can be interpreted as a term that takes into account the imperfections in the scaffold that gives rise to periodic collapse of bands of cells within the lattice as seen in Figs. 4 and 7. As the bands of cells collapse, the parameter  $A$  represents the magnitude of the collapse, and is hypothesized to be related to the layer height relative to the structure height. The parameter  $f$  represents the periodicity of such collapse events and is hypothesized to be related to the total number of layers in the structure.

## 4. Conclusions

In this study, we design and 3D print highly complex metallic microlattice structures with near-solid truss members having different unit-cell topologies designed to deform by bending and buckling-dominated mechanisms. The main conclusions are:

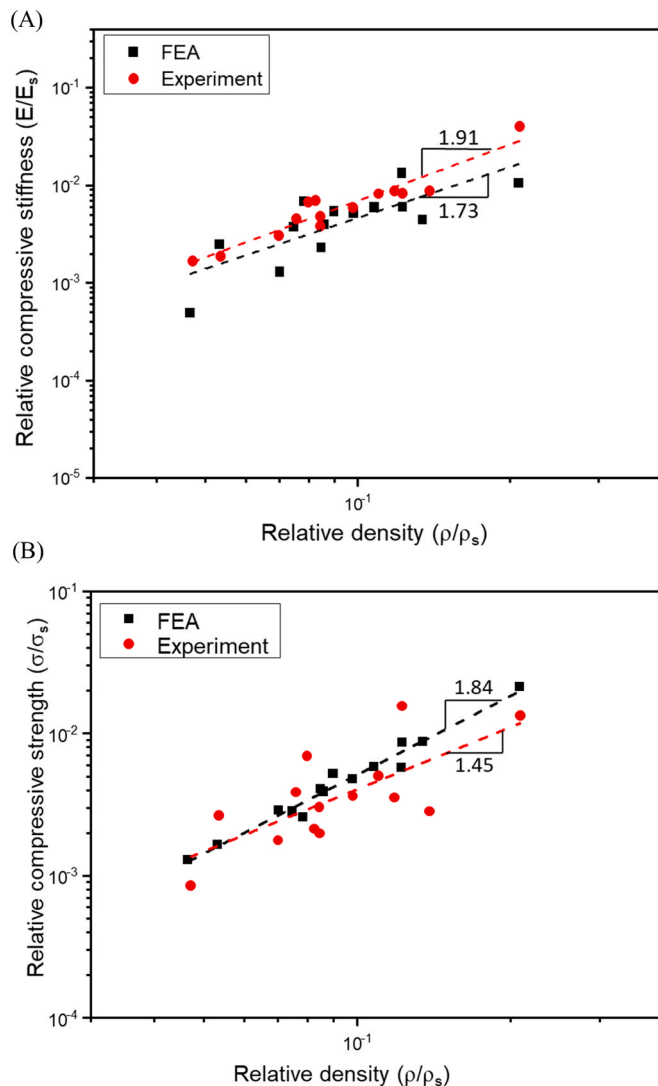


Fig. 8. FEA validation of mechanical response as a function of relative density. (A) Relative elastic modulus and (B) relative strength vs relative density for the octahedral samples and the corresponding FE models created with the same geometry as the experimental data.

- AJ nanoparticle 3D printing can be used to create metallic microlattices with near-solid truss members having diameters of 30–60  $\mu\text{m}$  with unit sizes in the range of 100–400  $\mu\text{m}$ . At this length scale, metallic lattices with near solid truss members have not been fabricated by any other technique, and this is the first report of their mechanical properties. The fabrication can be achieved by balancing the surface and inertia forces of the aerosolized microdroplets containing the metallic nanoparticles. The fabrication can thus be achieved in two simple steps of rapid droplet-based assembly (during printing) and sintering without the use of any sacrificial or support material.
- The microlattices fabricated in this work had an overall density of 5–26% of the bulk metal arising from a hierarchical porosity. The hierarchical porosity came from printing of the structure and sintering of the nanoparticles that form the truss members of the structure.
- Simple changes to the printing program were implemented to modulate the deformation behavior of the lattice structures from a purely bending-dominated (octahedral and hexagonal structures) to a combination of bending and buckling-dominated mechanisms (octahedral structure with central pillars).
- The stress-strain response of the microlattice structures under compression consists of an initial linear region up to a strain of 7–10%, followed by a long stress plateau characterized by periodic stress oscillations up to a strain of 50–70%, followed by rapid densification. This behavior is similar to that exhibited by macro-scale lattice structures reported in literature. The response is shown to be tunable in terms of relative stiffness (from 0.1% to 6.3%) and relative strength (from 0.2% to 9.0%). The periodic oscillations are within about 10% of the plateau stress for structures that exhibit bending-dominated deformation. The oscillation amplitude, however, increases to about 30% of the plateau stress when the deformation involves significant buckling within the layers. The former is characterized by periodically collapsing bands at about 30–45° to the horizontal. The latter, however, consists of layer-by-layer cascading collapse of the scaffold structures, with each failing layer being perpendicular to the direction of deformation.
- The stiffness and strength of the microlattice structures under compression depend primarily upon the relative density of the structures rather than the printing defects. Further, the scaling behavior of all the structures resembles that for bending-dominated structures, i.e.,  $(E/E_s) \propto (\rho/\rho_s)^2$  and  $(\sigma/\sigma_s) \propto (\rho/\rho_s)^{3/2}$ .
- Finite element models can capture both global stress-strain behavior of the structures including the elastic modulus and plateau stress, and a visual match in terms of deformation, bending, and collapse patterns of the experimental data. The agreement between FEA and experiments, however, is applicable to structures that deform by bending-dominated mechanism rather than a combination of bending and buckling-dominated mechanisms.
- A semi-empirical model has been proposed in this paper that can predict the stress-strain response of the cellular structures. Specifically, the model can predict the unique behavior of periodic softening and hardening in the plateau region of the stress-strain plot.

#### Funding

The authors gratefully acknowledge financial support from the National Science Foundation award no. CMMI-1757117.

#### Author contributions

R.P. came up with the concept and directed the research. M.S.S., C. H., and J.B. carried out AJ printing of the microlattices. M.S.S. and J.B. did imaging of the structures. M.S.S., A.M., and J.B. did the compression tests. C.H. carried out the FEA analysis, while J.B. worked on the theoretical model. All authors contributed to interpreting the data and

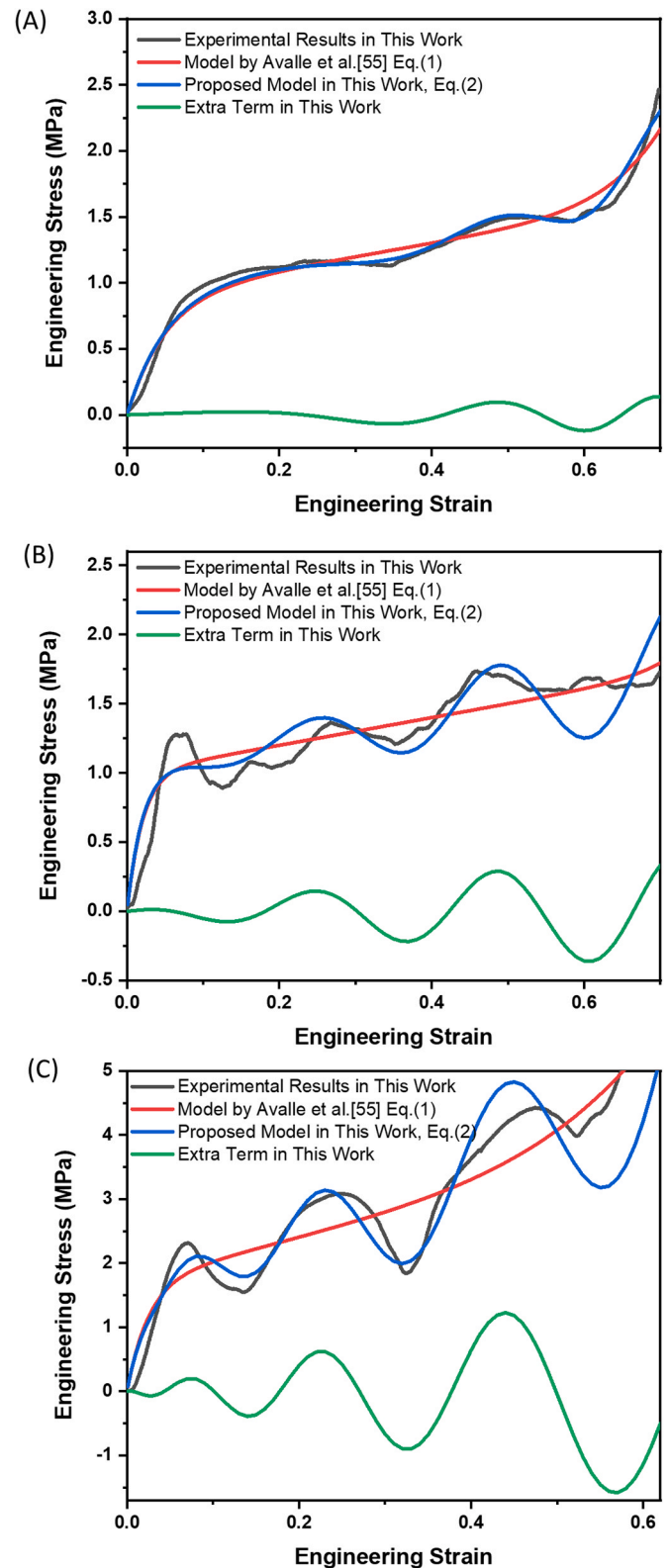


**Fig. 9. Modified theoretical model for stress vs strain behavior of cellular materials.** Theoretical model proposed in this work compared against the experimental data in this work and the model by Avalor et al. [55] for O-8(A), VP-2 (B) and HX-5(C). Our model can capture the periodic hardening and softening behavior in the stress-plateau region observed in the experiments. Models were fit manually with  $r^2$  values used to determine the quality of the fit.

preparing and editing the manuscript.

### Declaration of Competing Interest

The authors declare that they have no known competing financial interests or personal relationships that could have appeared to influence the work reported in this paper.

### Data and materials availability

All data needed to evaluate the conclusions in the paper are present in the paper and/or the Supporting Information. Additional data related to this paper may be requested from the authors.

### Acknowledgment

Part of the microscopy work was performed at the Nanoscience Fabrication and Characterization Facility at the University of Pittsburgh, under CMU-Pittsburgh collaborative agreement and the Franceschi Center at the Washington State University, Pullman WA.

### Appendix A. Supporting Information

Supplementary data associated with this article can be found in the online version at [doi:10.1016/j.addma.2021.101856](https://doi.org/10.1016/j.addma.2021.101856).

### References

- [1] S.C. Han, J.W. Lee, K. Kang, A new type of low density material: shellular, *Adv. Mater.* 27 (37) (2015) 5506–5511.
- [2] X. Zheng, H. Lee, T.H. Weisgraber, M. Shusteff, J. DeOtte, E.B. Duoss, J.D. Kuntz, M.M. Biener, Q. Ge, J.A. Jackson, Ultralight, ultrastiff mechanical metamaterials, *Science* 344 (6190) (2014) 1373–1377.
- [3] T. Frenzel, C. Findeisen, M. Kadic, P. Gumbsch, M. Wegener, Tailored buckling microlattices as reusable light-weight shock absorbers, *Adv. Mater.* 28 (28) (2016) 5865–5870.
- [4] M.S. Saleh, J. Li, J. Park, R. Panat, 3D printed hierarchically-porous microlattice electrode materials for exceptionally high specific capacity and areal capacity lithium ion batteries, *Addit. Manuf.* 23 (2018) 70–78.
- [5] A. Ataei, Y. Li, D. Fraser, G. Song, C. Wen, Anisotropic Ti-6Al-4V gyroid scaffolds manufactured by electron beam melting (EBM) for bone implant applications, *Mater. Des.* 137 (2018) 345–354.
- [6] M.V. Twigg, J.T. Richardson, Fundamentals and applications of structured ceramic foam catalysts, *Ind. Eng. Chem. Res.* 46 (12) (2007) 4166–4177.
- [7] P.H. Nam, P. Maiti, M. Okamoto, T. Kotaka, T. Nakayama, M. Takada, M. Ohshima, A. Usuki, N. Hasegawa, H. Okamoto, Foam processing and cellular structure of polypropylene/clay nanocomposites, *Polym. Eng. Sci.* 42 (9) (2002) 1907–1918.
- [8] C. Born, H. Kuckert, G. Wagner, D. Eifler, Ultrasonic torsion welding of sheet metals to cellular metallic materials, *Adv. Eng. Mater.* 5 (11) (2003) 779–786.
- [9] H.N. Wadley, Multifunctional periodic cellular metals, *Philos. Trans. R. Soc. A Math. Phys. Eng. Sci.* 364 (1838) (2006) 31–68.
- [10] J.A. Lewis, Direct ink writing of 3D functional materials, *Adv. Funct. Mater.* 16 (17) (2006) 2193–2204.
- [11] B.Y. Ahn, E.B. Duoss, M.J. Motala, X. Guo, S.-I. Park, Y. Xiong, J. Yoon, R.G. Nuzzo, J.A. Rogers, J.A. Lewis, Omnidirectional printing of flexible, stretchable, and spanning silver microelectrodes, *Science* 323 (5921) (2009) 1590–1593.
- [12] Y. Han, J. Dong, High-resolution direct printing of molten-metal using electrohydrodynamic jet plotting, *Manuf. Lett.* 12 (2017) 6–9.
- [13] S.H. Ko, J. Chung, N. Hotz, K.H. Nam, C.P. Grigoropoulos, Metal nanoparticle direct inkjet printing for low-temperature 3D micro metal structure fabrication, *J. Micromech. Microeng.* 20 (12) (2010), 125010.
- [14] C. Kullmann, N.C. Schirmer, M.-T. Lee, S.H. Ko, N. Hotz, C.P. Grigoropoulos, D. Poulidakos, 3D micro-structures by piezoelectric inkjet printing of gold nanofluids, *J. Micromech. Microeng.* 22 (5) (2012), 055022.
- [15] E. Sowade, M. Polomoshnov, A. Willert, R.R. Baumann, Toward 3D-printed electronics: inkjet-printed vertical metal wire interconnects and screen-printed batteries, *Adv. Eng. Mater.* 21 (10) (2019) 1900568.
- [16] D. Abueidda, M. Elhebeary, C.-S. (Andrew) Shiang, S. Pang, R.K. Abu Al-Rub, I. M. Jasiuk, Mechanical properties of 3D printed polymeric Gyroid cellular structures: experimental and finite element study, *Mater. Des.* 165 (2019), 107597.
- [17] L. Yang, O. Harrysson, H. West, D. Cormier, Compressive properties of Ti-6Al-4V auxetic mesh structures made by electron beam melting, *Acta Mater.* 60 (8) (2012) 3370–3379.
- [18] S. Tabacu, C. Ducu, Experimental testing and numerical analysis of FDM multi-cell inserts and hybrid structures, *Thin-Walled Struct.* 129 (2018) 197–212.
- [19] X. Zheng, W. Smith, J. Jackson, B. Moran, H. Cui, D. Chen, J. Ye, N. Fang, N. Rodriguez, T. Weisgraber, Multiscale metallic metamaterials, *Nat. Mater.* 15 (10) (2016) 1100–1106.
- [20] X. Yu, Y.J. Lee, R. Furstenberg, J.O. White, P.V. Braun, Filling fraction dependent properties of inverse opal metallic photonic crystals, *Adv. Mater.* 19 (13) (2007) 1689–1692.
- [21] R. Mines, On the characterisation of foam and micro-lattice materials used in sandwich construction 1, *Strain* 44 (1) (2008) 71–83.
- [22] S.L. Sing, J. An, W.Y. Yeong, F.E. Wiria, Laser and electron-beam powder-bed additive manufacturing of metallic implants: a review on processes, materials and designs, *J. Orthop. Res.* 34 (3) (2016) 369–385.
- [23] M.S. Saleh, C. Hu, R. Panat, Three-dimensional microarchitected materials and devices using nanoparticle assembly by pointwise spatial printing, *Sci. Adv.* 3 (3) (2017), e1601986.
- [24] T. Rahman, L. Renaud, D. Heo, M. Renn, R. Panat, Aerosol based direct-write micro-additive fabrication method for sub-mm 3D metal-dielectric structures, *J. Micromech. Microeng.* 25 (10) (2015), 107002.
- [25] M.T. Rahman, A. Rahimi, S. Gupta, R. Panat, Microscale additive manufacturing and modeling of interdigitated capacitive touch sensors, *Sens. Actuators A Phys.* 248 (2016) 94–103.
- [26] M.T. Rahman, C.-Y. Cheng, B. Karagoz, M. Renn, M. Schrandt, A. Gellman, R. Panat, High performance flexible temperature sensors via nanoparticle printing, *ACS Appl. Nano Mater.* 2 (5) (2019) 3280–3291.
- [27] L.J. Gibson, M.F. Ashby, *Cellular Solids: Structure and Properties*, Cambridge university press, 1999.
- [28] M.F. Ashby, The properties of foams and lattices, *Philos. Trans. R. Soc. A Math. Phys. Eng. Sci.* 364 (1838) (2006) 15–30.
- [29] Z. Hashin, S. Shtrikman, A variational approach to the theory of the elastic behaviour of multiphase materials, *J. Mech. Phys. Solids* 11 (2) (1963) 127–140.
- [30] S.D. Papka, S. Kyriakides, In-plane compressive response and crushing of honeycomb, *J. Mech. Phys. Solids* 42 (10) (1994) 1499–1532.
- [31] V.S. Deshpande, N.A. Fleck, M.F. Ashby, Effective properties of the octet-truss lattice material, *J. Mech. Phys. Solids* 49 (8) (2001) 1747–1769.
- [32] J. Berger, H. Wadley, R. McMeeking, Mechanical metamaterials at the theoretical limit of isotropic elastic stiffness, *Nature* 543 (7646) (2017) 533–537.
- [33] F. Habib, P. Iovenitti, S. Masood, M. Nikzad, D. Ruan, Design and evaluation of 3D printed polymeric cellular materials for dynamic energy absorption, *Int. J. Adv. Manuf. Technol.* 103 (5–8) (2019) 2347–2361.
- [34] C. Ling, A. Cernicchi, M.D. Gilchrist, P. Cardiff, Mechanical behaviour of additively-manufactured polymeric octet-truss lattice structures under quasi-static and dynamic compressive loading, *Mater. Des.* 162 (2019) 106–118.
- [35] K. Rusch, Energy-absorbing characteristics of foamed polymers, *J. Appl. Polym. Sci.* 14 (6) (1970) 1433–1447.
- [36] M. Avallé, G. Belingardi, A. Ibba, Mechanical models of cellular solids: parameters identification from experimental tests, *Int. J. Impact Eng.* 34 (1) (2007) 3–27.
- [37] L. Peroni, M. Avallé, M. Peroni, The mechanical behaviour of polyurethane foam: multiaxial and dynamic behaviour, *Int. J. Mater. Eng. Innov.* 1 (2) (2009) 154–174.
- [38] K.Y. Jeong, S.S. Cheon, M.B. Munshi, A constitutive model for polyurethane foam with strain rate sensitivity, *J. Mech. Sci. Technol.* 26 (7) (2012) 2033–2038.
- [39] V. Goga, B. Hücko, Phenomenological material model of foam solids, *Stroj. časopis - J. Mech. Eng.* 65 (1) (2015) 5–20.
- [40] B.K. Kim, J.U. Cho, K.Y. Jeong, Y. Chun, G.P. Carman, S.S. Cheon, A coupled constitutive relation with impulse-momentum for compressive impact behavior of the expanded polypropylene foam, *Polym. Eng. Sci.* 59 (1) (2019) 49–57.
- [41] M.T. Rahman, J. McCloy, C. Ramana, R. Panat, Structure, electrical characteristics, and high-temperature stability of aerosol jet printed silver nanoparticle films, *J. Appl. Phys.* 120 (7) (2016), 075305.
- [42] V. Crupi, E. Kara, G. Epasto, E. Guglielmino, H. Aykul, Static behavior of lattice structures produced via direct metal laser sintering technology, *Mater. Des.* 135 (2017) 246–256.
- [43] R.M. Latture, R.X. Rodriguez, L.R. Holmes Jr., F.W. Zok, Effects of nodal fillets and external boundaries on compressive response of an octet truss, *Acta Mater.* 149 (2018) 78–87.
- [44] C. Neff, N. Hopkinson, N.B. Crane, Experimental and analytical investigation of mechanical behavior of laser-sintered diamond-lattice structures, *Addit. Manuf.* 22 (2018) 807–816.
- [45] V. Deshpande, M. Ashby, N. Fleck, Foam topology: bending versus stretching dominated architectures, *Acta Mater.* 49 (6) (2001) 1035–1040.
- [46] M.S. Saleh, M. HamidVishkasogheh, H. Zbib, R. Panat, Polycrystalline micropillars by a novel 3-D printing method and their behavior under compressive loads, *Scr. Mater.* 149 (2018) 144–149.
- [47] Y. Gu, D. Gutierrez, S. Das, D.R. Hines, Inkwells for on-demand deposition rate measurement in aerosol-jet based 3D printing, *J. Micromech. Microeng.* 27 (9) (2017).
- [48] G. Chen, Y. Gu, H. Tsang, D.R. Hines, S. Das, The effect of droplet sizes on overspray in aerosol-jet printing, *Adv. Eng. Mater.* 20 (8) (2018) 1701084.
- [49] R. Dou, B. Xu, B. Derby, High-strength nanoporous silver produced by inkjet printing, *Scr. Mater.* 63 (3) (2010) 308–311.
- [50] M.T. Rahman, R. Moser, H.M. Zbib, C. Ramana, R. Panat, 3D printed high performance strain sensors for high temperature applications, *J. Appl. Phys.* 123 (2) (2018), 024501.
- [51] H. Yang, M.T. Rahman, D. Du, R. Panat, Y. Lin, 3-D printed adjustable microelectrode arrays for electrochemical sensing and biosensing, *Sens. Actuators B Chem.* 230 (2016) 600–606.

- [52] M.A. Ali, C. Hu, S. Jahan, B. Yuan, M.S. Saleh, E. Ju, S.-J. Gao, R.P. Panat, Sensing of COVID-19 antibodies in seconds via aerosol jet printed three dimensional electrodes, *Adv. Mater.* (2020), 202006647.
- [53] H. Fan, F. Jin, D. Fang, Characterization of edge effects of composite lattice structures, *Compos. Sci. Technol.* 69 (11–12) (2009) 1896–1903.
- [54] H. Lyu, M. Hamid, A. Ruimi, H.M. Zbib, Stress/strain gradient plasticity model for size effects in heterogeneous nano-microstructures, *Int. J. Plast.* 97 (2017) 46–63.
- [55] M. Avalle, G. Belingardi, A mechanical model of cellular solids for energy absorption, *Adv. Eng. Mater.* 21 (4) (2019) 1800457.